Cylindrical Radial Filter Design with Application to Local Wave Field Synthesis

Nara Hahn, Frank Schultz, and Sascha Spors

***Abstract*—The cylindrical radial filters refer to the discrete-time realizations of the radially dependent parts in cylindrical harmonic expansions. described by the Bessel functions. An efficient and accurate design of the radial filters is crucial in spatial signal processing applications such as sound field synthesis and active noise control. We present a radial filter design method where the filter coefficients are analytically derived from the time-domain representations. Time-domain sampling of the cylindrical radial functions typically leads to spectral aliasing artifacts and degrades the accuracy of the filter. This is mainly attributed to the unbounded discontinuities exhibited by the time-domain radial functions. This problem is coped with by exploiting an approximation where the cylindrical radial function is represented as a weighted sum of the radial functions in spherical harmonic expansions. Although the spherical radial functions also exhibit discontinuities in the time domain, the amplitude remains finite which allows to apply a recently introduced aliasing reduction method. The proposed cylindrical radial filter is designed by linearly combining the spherical radial filters with improved accuracy. We demonstrate the performance of the proposed cylindrical radial filters by examining the spectral deviations from the original spectrum.**

I. INTRODUCTION

The spherical and cylindrical harmonic representations of wave fields are commonly used in spatial sound field analysis and reproduction [1–6]. The directional component of the sound field is expressed in terms of spherical and cylindrical harmonics, whereas the radial dependencies are described by the spherical and cylindrical Bessel and Hankel functions. For the discrete-time modeling and manipulation of the modal representations, their respective radial functions have to be realized as digital filters. We refer to these as the radial filters in the remainder.

The discrete-time implementation of the radial functions is often performed by sampling the frequency-domain representations. This, however, requires the evaluation of the Bessel and Hankel functions for every frequency bin which is computationally demanding. Moreover, the inverse discrete Fourier transform of the sampled spectrum typically results in temporally aliased signals. It also introduces a substantial amount of group delay which makes the frequency-domain approach not suited for real-time applications.

Recently, the time-domain realization of the radial filters has been studied to overcome these disadvantages, with the focus being predominantly on the spherical radial filters. Instead of relying on traditional filter design algorithms (e.g. least squares), the filter coefficients are derived analytically from the mathematical expressions describing the radial functions. Since the coefficients are given in closed form, the filter design can be carried out efficiently. This facilitates the real-time implementation of spatial signal processing applications. The radial filters associated with the spherical Hankel functions have been commonly realized as infinite impulse response (IIR) filters whose design bases on the explicit series expansions in the Laplace domain [7–11]. For homogeneous sound fields, the time-domain radial functions are described by polynomials within a finite temporal support and equal to zero elsewhere [12–15]. Due to this temporal property, the corresponding radial filters are often realized as finite impulse response (FIR) filters [16–18]. The FIR coefficients are commonly obtained by directly sampling the time-domain representations of the radial function. The spectral accuracy of such filters, however, suffers from spectral aliasing which originates from the infinite bandwidth of the radial function. In [19], we investigated the temporal and spectral artifacts resulting from the time-domain sampling of the spherical radial filters for varying physical variables and design parameters. An improved radial filter design was proposed in [20, 21] where the discontinuities occurring in the time domain are substituted by analytically derived band limited jump functions, thereby reducing the aliasing artifacts. Since the band limitation exploits polynomial interpolation kernels, the radial filter coefficients are given in closed form.

The design of cylindrical radial filters in the time domain has been relatively unexplored. Although the explicit expressions for the time-domain radial functions are known [22], it is not trivial to achieve a reasonable spectral accuracy. This is mainly due to the slow decay of the spectrum towards high frequencies which causes strong aliasing artifacts if sampled in the time domain. The band limitation approach employed for the spherical radial filters cannot be applied here, since the amplitude of the time-domain radial functions exhibits unbounded discontinuities. The straightforward solution of increasing the sampling rate comes at the expense of computational cost. In [22], a nonlinear amplitude mapping was applied to the time-domain cylindrical radial functions which effectively reduced the aliasing distortions. However, the downside of this approach is that the nonlinear mapping function has to be chosen heuristically.

This article proposes a new time-domain design of the cylindrical radial filters. The FIR coefficients are given in

This is the author manuscript of the article published in the *Journal of the Audio Engineering Society* on 10th June 2022, available at: https://doi.org/10.17743/jaes.2022.0013.)

closed form which are derived analytically from the time-domain representations of the radial functions. Based on the mathematical expressions of the spherical and cylindrical harmonic expansions (Sec. II-A, Sec. II-B and Sec. II-C), the cylindrical radial functions are approximated in terms of the spherical radial functions (Sec. II-D). The temporal and spectral properties of the approximation are investigated with our focus on modal truncation and modal windowing. By exploiting the approximation, the cylindrical radial filters are constructed by linearly combining the spherical radial filters (Sec. III). The individual spherical radial filters are designed by employing the band-limitation approach summarized in Sec. III-A. The improved accuracy of the proposed cylindrical radial filters are evaluated in Sec. III-B in terms of spectral deviations and normalized squared errors. As a use case, the wave field synthesis (WFS) driving functions for virtual plane waves are computed by using the proposed cylindrical radial filters (Sec. IV). The spatial structure and the spectral properties of the synthesized sound fields are presented, demonstrating the benefits of the presented approach.

II. CYLINDRICAL AND SPHERICAL HARMONIC REPRESENTATIONS

This section reviews the cylindrical and spherical harmonic expansions of plane waves. Based on these representations, the relation between the cylindrical and spherical radial function is derived. This will be exploited in the design of the cylindrical radial filters in Sec. III.

We consider the sound field of a plane wave driven by a Dirac impulse $\delta(t)$. The sound field is evaluated at a point denoted by $\boldsymbol{x} = (r\sin\theta\cos\phi, r\sin\theta\sin\phi, r\cos\theta)^{\mathrm{T}}$ where r, θ, and ϕ respectively denote radius, colatitude and azimuth angle. The plane wave is assumed to propagate parallel to the xy plane, where the propagating direction is denoted by the unit vector $\boldsymbol{n}_{\mathrm{pw}} = (\cos\phi_{\mathrm{pw}}, \sin\phi_{\mathrm{pw}}, 0)^{\mathrm{T}}$ with ϕ_{pw} denoting the azimuth angle. The time in second is denoted by t and the angular frequency by $\omega = 2\pi f$ with f denoting the frequency in Hertz. The scalar product of $\boldsymbol{x}$ and $\boldsymbol{n}_{\mathrm{pw}}$ is denoted by $\langle \boldsymbol{x}, \boldsymbol{n}_{\mathrm{pw}} \rangle$. In frequency-domain expressions, the time harmonic term $e^{i\omega t}$ is omitted for brevity. The imaginary unit is denoted by i and the speed of sound in $\mathrm{m/s}$ by c. In numerical simulations, the speed of sound is set to $c = 343\,\mathrm{m/s}$.

A. Cylindrical Harmonic Expansion

In the frequency domain, the sound field of the plane wave can be expressed in terms of cylindrical harmonics by using the Jacobi-Anger expansion [23, p. 687],

$$e^{-i\frac{\omega}{c}\langle \boldsymbol{x}, \boldsymbol{n}_{\mathrm{pw}} \rangle} = \sum_{m=-\infty}^{\infty} \underbrace{i^{-m} J_m(\tfrac{\omega}{c}\rho)}_{\substack{\text{frequency-domain} \\ \text{radial function}}} e^{im(\phi - \phi_{\mathrm{pw}})}, \tag{1}$$

where $J_m(\cdot)$ denote the cylindrical Bessel functions of the first kind. For brevity, the radial distance from the z axis is denoted by $\rho := r\sin\theta = \sqrt{x^2 + y^2}$. The underbraced term represents the radius- and frequency-dependent part of each cylindrical mode. The time-domain representation of the plane wave in the cylindrical harmonics domain reads [22, Eq. (4)]

$$\delta\left(t - \tfrac{1}{c}\langle \boldsymbol{x}, \boldsymbol{n}_{\mathrm{pw}} \rangle\right) = \begin{cases} \displaystyle\sum_{m=-\infty}^{\infty} \underbrace{\frac{c}{\pi\rho} \frac{T_m(\frac{ct}{\rho})}{\sqrt{1 - (\frac{ct}{\rho})^2}}}_{\substack{\text{time-domain} \\ \text{radial function}}} e^{im(\phi - \phi_{\mathrm{pw}})}, & \left|\frac{ct}{\rho}\right| \leq 1 \\ 0, & \left|\frac{ct}{\rho}\right| > 1, \end{cases} \tag{2}$$

where $T_m(\cdot)$ denote the Chebyshev polynomials of the first kind. This follows from the Fourier transform relation of the respective radial functions [24, Eq. (11.4.24)],

$$\mathcal{F}^{-1}\left\{ i^{-m} J_m(\tfrac{\omega}{c}\rho) \right\} = \begin{cases} \frac{c}{\pi\rho} \frac{T_m(\frac{ct}{\rho})}{\sqrt{1 - (\frac{ct}{\rho})^2}}, & \left|\frac{ct}{\rho}\right| \leq 1 \\ 0, & \left|\frac{ct}{\rho}\right| > 1 \end{cases}, \tag{3}$$

with $\mathcal{F}^{-1}\{\cdot\}$ denoting the inverse Fourier transform. Equation (2) constitutes a Chebyshev series expansion of the Dirac delta function, where $1/\sqrt{1 - (c\,t/\rho)^2}$ corresponds to the weighting function with respect to which the Chebyshev polynomials are orthogonal within $|\frac{ct}{\rho}| \leq 1$ [25, Ch. 18]. Please note that the symbol $T_m(\frac{ct}{\rho})$ will be used to represent Chebyshev polynomials windowed by a rectangular pulse in the remainder. The finite temporal support within $|\frac{ct}{\rho}| \leq 1$ is implicitly assumed, and the expression for the zero part (i.e. $|\frac{ct}{\rho}| > 1$) will be omitted for brevity.

The frequency- and time-domain cylindrical radial functions are respectively depicted in Fig. 1(a) and Fig. 1(c) for $\theta = \frac{\pi}{2}$ (i.e. $\rho = r$). It can be seen that the high-frequency spectra ($\frac{\omega}{c} r > m$) are decaying at the rate of $-10\,\mathrm{dB/decade}$. At $\omega = 0$, the magnitude of the zeroth-order radial function is $0\,\mathrm{dB}$ whereas higher-order ($m \geq 1$) radial functions exhibit mth-order zero(s). The time-domain cylindrical radial functions have a finite temporal support and exhibit two discontinuities at $|t| = \frac{r}{c}$. The time-domain amplitude tends to infinity as $|t| \to \frac{r}{c}$ which is attributed to the square root term in the denominator of the time-domain radial function. Due to the even/odd symmetry of time-domain radial functions of even/odd orders, the corresponding frequency-domain radial functions are purely real/imaginary [26, Sec. 9.5.3].

B. Spherical Harmonic Expansion

The same sound field can be expressed in the spherical harmonics domain, where the frequency-domain representation reads [1, Eq. (6.175)]

$$e^{-i\frac{\omega}{c}\langle \boldsymbol{x}, \boldsymbol{n}_{\mathrm{pw}} \rangle} = 4\pi \sum_{n=0}^{\infty} \underbrace{i^{-n} j_n(\tfrac{\omega}{c} r)}_{\substack{\text{frequency-domain} \\ \text{radial function}}} \sum_{m=-n}^{n} Y_{nm}(\theta, \phi) Y_{nm}^*(\tfrac{\pi}{2}, \phi_{\mathrm{pw}}), \tag{4}$$

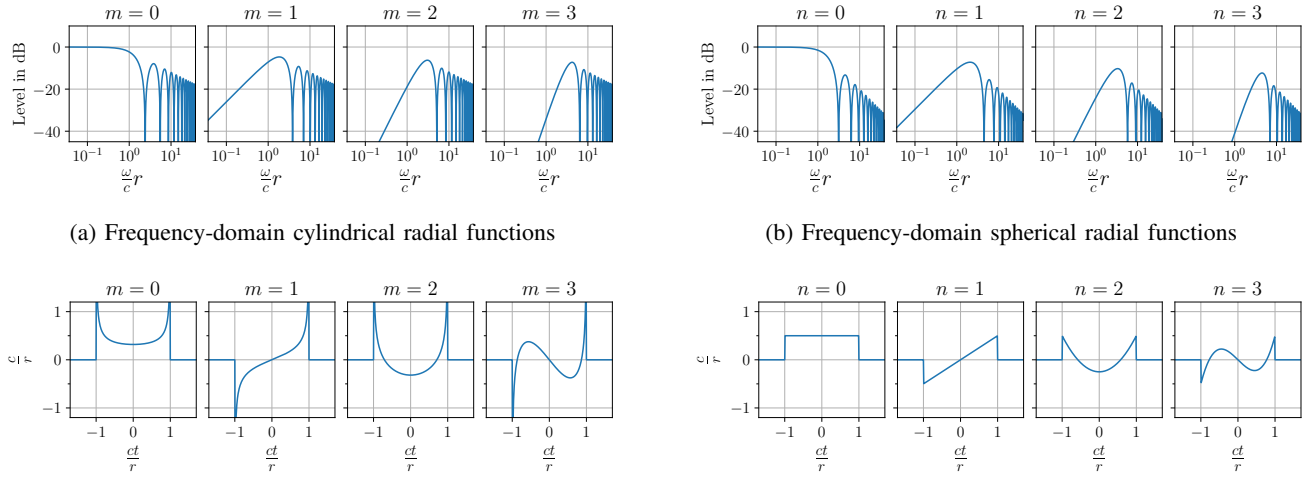

(a) Frequency-domain cylindrical radial functions

(b) Frequency-domain spherical radial functions

(c) Time-domain cylindrical radial functions

(d) Time-domain spherical radial functions

Fig. 1: Radial functions for cylindrical (left column) and spherical (right column) harmonic expansions. The frequency axes are scaled by $\frac{r}{c}$ and the time axes by $\frac{c}{r}$.

with $j_n(\cdot)$ denoting the spherical Bessel functions of the first kind. The spherical harmonics are denoted by $Y_{nm}(\cdot,\cdot)$ and defined as [25, Eq. (14.30.1)]

$$Y_{nm}(\theta,\phi) = \sqrt{\frac{2n+1}{4\pi}\frac{(n-m)!}{(n+m)!}} P_n^m(\cos\theta) e^{im\phi} \tag{5}$$

with $P_n^m(\cdot)$ denoting the associated Legendre functions. The Condon-Shortley phase term $(-1)^m$ is included in $P_n^m(\cdot)$. The asterisk in the superscript $(\cdot)^*$ denotes the complex conjugate. The time-domain spherical harmonic expansion of the plane wave reads [18]

$$\delta\left(t - \tfrac{1}{c}\langle \boldsymbol{x}, \boldsymbol{n}_{\text{pw}}\rangle\right) \tag{6}$$
$$= \begin{cases} 4\pi \sum_{n=0}^{\infty} \underbrace{\frac{c}{2r} P_n(\frac{c}{r}t)}_{\substack{\text{time-domain}\\ \text{radial function}}} \sum_{m=-n}^{n} Y_{nm}(\theta,\phi) Y_{nm}^*(\tfrac{\pi}{2},\phi_{\text{pw}}), & \left|\tfrac{c}{r}t\right| \le 1 \\ 0, & \left|\tfrac{c}{r}t\right| > 1, \end{cases}$$

where $P_n(\cdot)$ denote the Legendre polynomials. The individual modes satisfy the Fourier transform relation

$$\mathcal{F}^{-1}\left\{i^{-n} j_n(\tfrac{\omega}{c}r)\right\} = \begin{cases} \frac{c}{2r} P_n(\frac{c}{r}t), & \left|\tfrac{c}{r}t\right| \le 1 \\ 0, & \left|\tfrac{c}{r}t\right| > 1. \end{cases} \tag{7}$$

Equation (6) constitutes the Legendre series expansion of the Dirac delta function [25, Ch. 18]. Please note that the symbol $P_n(\frac{c}{r}t)$ represents a windowed Legendre polynomial within $|\frac{c}{r}t| \le 1$ in the remainder. The finite temporal support is thereby assumed and the expression for $|\frac{c}{r}t| > 1$ will be omitted.

The frequency- and time-domain spherical radial functions are depicted in Fig. 1(b) and Fig. 1(d), respectively. It can be seen that the spectra at high frequencies ($\frac{\omega}{c}r > n$) decay at the rate of $-20\,\text{dB/decade}$, i.e. twice as steep as for the cylindrical radial functions. At $\omega = 0$ the zeroth-order radial function has $0\,\text{dB}$ gain whereas higher-order ($n \ge 1$) radial functions exhibit nth-order zero(s). The time-domain spherical radial functions have also a finite temporal extent within $|t| < \frac{r}{c}$ and exhibit discontinuities at the edges $|t| = \frac{r}{c}$. Unlike the cylindrical case, the amplitude of the time-domain radial functions is always finite. Since even/odd-order radial functions are even/odd symmetric in the time domain, the corresponding frequency-domain radial functions are purely real/imaginary.

C. Explicit Relation of the Radial Functions

In order to derive the relation of the cylindrical and spherical radial functions, the respective time-domain expansions (2) and (6) are compared for $\theta = \frac{\pi}{2}$ (i.e. $\rho = r$). The order in the double sum (6) is exchanged,

$$\delta\left(t - \tfrac{1}{c}\langle \boldsymbol{x}, \boldsymbol{n}_{\text{pw}}\rangle\right) \tag{8}$$
$$= 4\pi \sum_{m=-\infty}^{\infty} e^{im(\phi-\phi_{\text{pw}})} \sum_{n=|m|}^{\infty} \frac{c}{2r} P_n(\tfrac{c}{r}t) Y_{nm}(\tfrac{\pi}{2},0) Y_{nm}^*(\tfrac{\pi}{2},0).$$

We used the relations $Y_{nm}(\frac{\pi}{2},\phi) = Y_{nm}(\frac{\pi}{2},0)e^{im\phi}$ and $Y_{nm}^*(\frac{\pi}{2},\phi_{\text{pw}}) = Y_{nm}(\frac{\pi}{2},0)e^{-im\phi_{\text{pw}}}$ following from (5). Comparing the addends (mth term) of (8) with (2) yields

$$\frac{c}{\pi r}\frac{T_m(\frac{c}{r}t)}{\sqrt{1-(\frac{c}{r}t)^2}}$$
$$= 4\pi \sum_{n=|m|}^{\infty} \frac{c}{2r} P_n(\tfrac{c}{r}t) Y_{nm}(\tfrac{\pi}{2},0) Y_{nm}^*(\tfrac{\pi}{2},0) \tag{9}$$
$$= \sum_{n=|m|}^{\infty} (2n+1)\frac{c}{2r} P_n(\tfrac{c}{r}t)\frac{(n-m)!}{(n+m)!}[P_n^m(0)]^2 \tag{10}$$
$$= \sum_{n=|m|}^{\infty} (2n+1)\frac{c}{2r} P_n(\tfrac{c}{r}t) K_n^m, \tag{11}$$

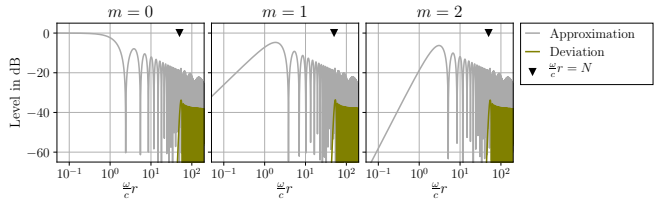

(a) Frequency domain ($N = 50$, $\beta = 0$)

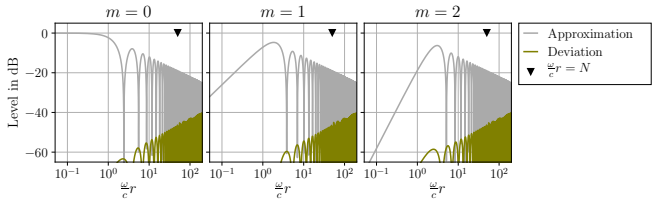

(b) Frequency domain ($N = 50$, $\beta = 4$)

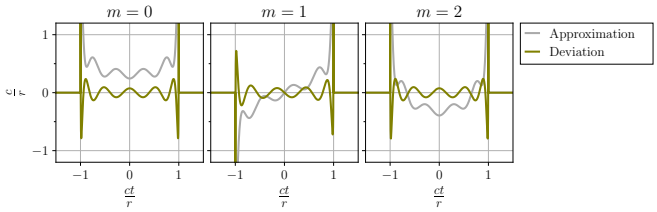

(c) Time domain ($N = 10$, $\beta = 0$)

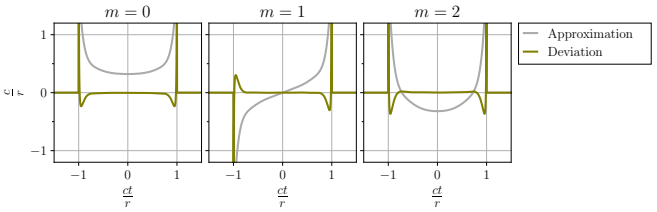

(d) Time domain ($N = 10$, $\beta = 4$)

Fig. 2: Approximation of the cylindrical radial functions by using the spherical radial functions (18). The maximum spherical harmonics order N is set to 50 for the frequency domain and 10 for the time domain. A rectangular modal window ($\beta = 0$) is used in (a) and (c) and a Kaiser-Bessel modal window with $\beta = 4$ in (b) and (d).

where (5) is exploited in the second equality. The coefficient K_n^m is defined as [27, Eq. (19)]

$$K_n^m := \frac{(n-m)!}{(n+m)!}[P_n^m(0)]^2 \tag{12}$$

$$= \begin{cases} \frac{(n-m-1)!!(n+m-1)!!}{(n+m)!!(n-m)!!}, & n+m \text{ even} \\ 0, & n+m \text{ odd}, \end{cases} \tag{13}$$

where $(\cdot)!!$ denotes the double factorial. The second equality in (13) follows from [23, p. 783],

$$P_n^m(0) = \begin{cases} (-1)^{\frac{n-m}{2}} \frac{(n+m-1)!!}{(n-m)!!}, & n+m \text{ even} \\ 0, & n+m \text{ odd}. \end{cases} \tag{14}$$

The double factorial coefficient K_n^m can be computed recursively by exploiting $K_0^0 = 1$ and

$$K_n^m = \frac{n+m-1}{n+m} K_{n-1}^{m-1} \tag{15}$$

$$K_n^m = \frac{n-m-1}{n-m} K_{n-1}^{m+1}. \tag{16}$$

The frequency-domain representation of (11) can be obtained by replacing the time-domain radial functions with their Fourier transforms (cf. (3) and (7)), yielding [28, Appendix]

$$i^{-m} J_m(\tfrac{\omega}{c}r) = \sum_{n=|m|}^{\infty} (2n+1) i^{-n} j_n(\tfrac{\omega}{c}r) K_n^m. \tag{17}$$

Equation (11) and (17) represent the cylindrical radial functions as a linear combination of the spherical radial functions ($n \geq |m|$) in the respective domain. Since the mth cylindrical radial function exhibits $|m|$th-order zeros at $\omega = 0$ (cf. Fig. 1(a)), the lowest spherical radial function order used in the approximation is $n = |m|$ which exhibit the same order of zeros at $\omega = 0$. Lower-order ($n < |m|$) spherical radial functions are not used. Note from (13) that K_n^m is nonzero only if $n + m$ is even (i.e. both n and m are either even or odd integers). This means that (11) or (17) expresses an even/odd-order cylindrical radial function with even/odd-order spherical radial functions. Recall from Fig. 1(c) and Fig. 1(d) that the time-domain radial function are even/odd symmetric for even/odd orders. In the frequency domain, this corresponds to the purely real/imaginary spectra of even/odd-order radial functions. The cylindrical radial function of a given order is therefore expressed as a linear combination of spherical radial functions having the same time-domain symmetry, or equivalently, exhibiting purely real/imaginary spectra.

D. Approximation

For practical usage, the explicit expression (11) has to be truncated to a finite sum,

$$\frac{c}{\pi r} \frac{T_m(\frac{ct}{r})}{\sqrt{1-(\frac{ct}{r})^2}} \approx \frac{c}{2r} \sum_{n=|m|}^{N} W_n \cdot (2n+1) P_n(\tfrac{c}{r}t) K_n^m, \tag{18}$$

where N denotes the maximum spherical harmonic order. We consider this as the approximation of the cylindrical radial functions in terms of the spherical radial functions. The number of nonzero terms in (18) is $\lceil \frac{N-|m|+1}{2} \rceil$ with $\lceil \cdot \rceil$ denoting the ceiling function. In order to mitigate the effect of hard modal truncation, a window W_n is introduced for modal smoothing. In this paper, we use the right half of the Kaiser-Bessel window for modal windowing [29],

$$W_n = \frac{I_0\left(\beta\sqrt{1-(\frac{n-|m|}{N-|m|})^2}\right)}{I_0(\beta)}, \tag{19}$$

where $n = |m|, |m|+2, \ldots, N$ and $I_0(\cdot)$ denotes the zeroth-order modified Bessel function. The parameter $\beta \geq 0$

determines the shape of the modal window with $\beta = 0$ corresponding to the rectangular window.

The approximated cylindrical radial functions are depicted in Fig. 2. The approximations without modal smoothing ($\beta = 0$) are shown in Fig. 2(a). The spectra are accurate for $\frac{\omega}{c}r < N$ and the spectral deviation (indicated by olive curves) are mainly found at high frequencies ($\frac{\omega}{c}r > N$). The effect of using a modal window ($\beta = 4$) in the frequency domain is illustrated in Fig. 2(b). Although the spectral deviations are distributed throughout a wider frequency range, the magnitude spectrum (gray) is more accurately approximated. Figure 2(c) shows the time-domain radial functions without modal windowing ($\beta = 0$). The time-domain deviations exhibit strong oscillatory behavior which agrees with the steep high pass filtered characteristic of their spectra (cf. the spectral deviations depicted in Fig. 2(a)). This is moderated by the modal weighting ($\beta = 4$) as shown in Fig. 2(d). Note that the approximation is qualitatively similar to the original radial functions (cf. Fig. 1(c)).

III. RADIAL FILTER DESIGN

In this section, we discuss the discrete-time modeling of the cylindrical and spherical radial functions. Since the time-domain radial functions are of finite length (cf. Fig. 1(c) and Fig. 1(d)), it appears reasonable to realize them as FIR filters. A direct sampling of the time-domain radial functions, however, leads to a poor modeling accuracy. This is due to the infinite bandwidth of the radial functions as depicted in Fig. 1(a) and Fig. 1(b). Sampling these functions in the time domain inevitably causes spectral aliasing. For the spherical radial filters, the resulting aliasing artifacts have been investigated in [19]. A spherical radial filter design with reduced aliasing was recently presented in [20, 21].

The time-domain sampling of the cylindrical radial filter gives rise to more severe aliasing. This is mainly due to the slower decay of the high frequency spectrum as shown in Fig. 1(a). Figure 3 depicts the artifacts that results from time-domain sampling. Because of the diverging amplitude around $|t| = \frac{r}{c}$, the energy of the cylindrical radial functions is over- or underestimated depending on the fractional part of $\frac{r}{cT_\mathrm{s}}$ (cf. Fig. 3(a)) with $T_\mathrm{s} := \frac{1}{f_\mathrm{s}}$ denoting the sampling period. Moreover, since the temporal extent of the radial functions is not properly modeled, the notch frequencies do not match with the original spectrum (cf. Fig. 3(b)). This problem was reported in [22] where the cylindrical radial filters are used for the derivation of wave field synthesis driving functions. The authors employed a heuristically chosen nonlinear amplitude mapping function in order to reduce this spectral deviation.

In the present article, we propose an improved cylindrical radial filter design which combines the approximation presented in Sec. II-D and the spherical radial filter design method introduced in [21]. Section III-A briefly introduces the design of spherical filters with reduced aliasing. The spherical radial filters are then linearly combined to design improved cylindrical radial filters (Sec. III-B). The validity of this approach is demonstrated by numerical results.

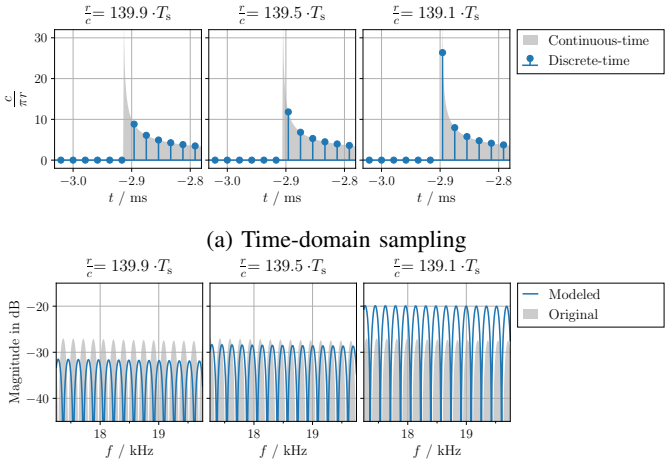

(a) Time-domain sampling

(b) Frequency responses

Fig. 3: Time-domain sampling of the zeroth-order cylindrical radial function ($f_\mathrm{s} = 48\,\mathrm{kHz}$). The sampled values around $t = -\frac{r}{c}$ are shown in (a) for varying $\frac{r}{c}$. The resulting high-frequency responses are compared with the original spectrum (gray) in (b).

A. Spherical Radial Filter Design

This section reviews a recent spherical radial filter design method [21]. The spectral aliasing resulting from time-domain sampling is reduced by applying an analytical low-pass filter to the radial functions. The FIR coefficients of the radial filters are then obtained by sampling the low-pass filtered expressions. Due to the attenuation of the spectral components beyond the base band (i.e. $|f| > \frac{f_\mathrm{s}}{2}$), the resulting filters exhibit reduced aliasing artifacts. The original idea of the analytical band limitation is primarily introduced for the digital emulation of analog synthesizer sounds such as triangular, rectangular and sawtooth waves [30–33]. Only the zeroth- and first-order discontinuities have been of interest there. This approach has also been employed for modeling nonlinear analog systems like hard/soft clipping [34–36]. The aliasing artifacts are reduced by applying a band limitation to the first- and second-order discontinuities. The band limitation of higher-order discontinuities are presented in [21, 37] which was employed for the design of spherical radial filters. Please refer to [21] for a more comprehensive treatment of this approach.

Let us first consider the zeroth-order case where the time-domain radial function is a rectangular pulse (cf. Fig. 1(d)). It can be expressed as

$$P_0(\tfrac{c}{r}t) = u(t + \tfrac{r}{c}) - u(t - \tfrac{r}{c}) \tag{20}$$

$$= \int_{-\infty}^{t} \Big[\delta(t' + \tfrac{r}{c}) - \delta(t' - \tfrac{r}{c})\Big] \mathrm{d}t', \tag{21}$$

with $u(\cdot)$ denoting the Heaviside step function. Recall that $P_n(\cdot)$ is a windowed Legendre polynomial. The amplitude $\frac{c}{2r}$ is dropped here for brevity. In the second equality, each unit step function is expressed as an integral over the shifted

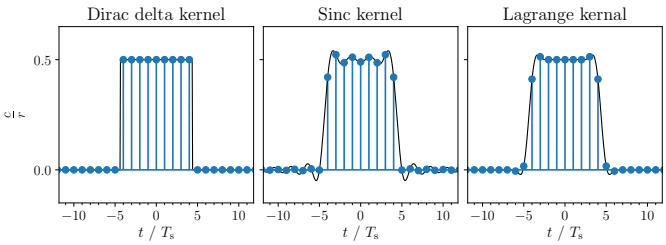

Fig. 4: The zeroth-order spherical radial filters ($\frac{r}{c} \approx 4.373 \cdot T_\mathrm{s}$). The jump discontinuities at $|t| = \frac{r}{c}$ are realized as the running integral of different kernels. Left: Dirac delta kernel (full band). Center: Sinc kernel (ideal band limitation). Right: Lagrange kernel (third order).

Dirac delta function $\delta(t \pm \frac{r}{c})$. In order to reduce the spectral components at high frequencies, (21) is convolved with the impulse response $h(t)$ of a low pass filter, yielding

$$h(t) * P_0(\tfrac{c}{r}t) = \int_{-\infty}^{t} \Big[h(t' + \tfrac{r}{c}) - h(t' - \tfrac{r}{c})\Big] \mathrm{d}t' \tag{22}$$

$$= H_0(t + \tfrac{r}{c}) - H_0(t - \tfrac{r}{c}), \tag{23}$$

where $H_0(t)$ denotes the antiderivative of $h(t)$,

$$H_0(t) \coloneqq \int_{-\infty}^{t} h(t') \mathrm{d}t'. \tag{24}$$

The latter is called the band-limited step function in the literature, cf. [31].

The impulse response of an ideal anti-aliasing filter is the sinc function $h^{(\mathrm{sinc})}(t) = \mathrm{sinc}(f_\mathrm{s} \cdot t) = \frac{\sin(\pi f_\mathrm{s} t)}{\pi f_\mathrm{s} t}$. The corresponding band-limited step function reads [25, Eq. (6.2.10)][33, Eq. (10)]

$$H_0^{(\mathrm{sinc})}(t) = \int_{-\infty}^{t} \mathrm{sinc}(f_\mathrm{s} \cdot t') \mathrm{d}t' = \frac{1}{2} + \frac{1}{\pi} \mathrm{Si}(\pi f_\mathrm{s} t), \tag{25}$$

where $\mathrm{Si}(\cdot)$ denotes the sine integral function. Figure 4 (left and center) depicts the zeroth-order radial function before and after the band limitation. Due to the ideal low-pass filtering, the band-limited radial filter exhibits infinitely long temporal extent.

Next, we consider the first-order case ($n = 1$) where the time-domain radial function is described by a linear function within $|t| < \frac{r}{c}$. Note from Fig. 1(d) that not only the signal but also its derivative are discontinuous at $|t| = \frac{r}{c}$. The first-order radial function is thus expressed as

$$P_1(\tfrac{c}{r}t) = -u(t + \tfrac{r}{c}) - u(t - \tfrac{r}{c}) \tag{26}$$
$$+ \tfrac{c}{r}(t + \tfrac{r}{c}) \cdot u(t + \tfrac{r}{c}) - \tfrac{c}{r}(t - \tfrac{r}{c}) \cdot u(t - \tfrac{r}{c}).$$

The zeroth-order discontinuities are described by $u(t \pm \frac{r}{c})$ whereas the first-order discontinuities by the ramp functions $(t \pm \frac{r}{c}) \cdot u(t \pm \frac{r}{c})$. The scaling factor $\frac{c}{r}$ represents the magnitude of the first-order discontinuities. Again, the amplitude $\frac{c}{2r}$ is omitted for brevity. Since the ramp function can be expressed as the second-order antiderivative of $\delta(t)$,

$$(t \pm \tfrac{r}{c}) \cdot u(t \pm \tfrac{r}{c}) = \int_{-\infty}^{t} \left(\int_{-\infty}^{t'} \delta(t'' \pm \tfrac{r}{c}) \mathrm{d}t'' \right) \mathrm{d}t', \tag{27}$$

(26) can be rewritten as

$$P_1(\tfrac{c}{r}t) = \int_{-\infty}^{t} \Big[-\delta(t + \tfrac{r}{c}) - \delta(t - \tfrac{r}{c}) \Big] \mathrm{d}t' \tag{28}$$
$$+ \frac{c}{r} \int_{-\infty}^{t} \left(\int_{-\infty}^{t'} \Big[\delta(t'' + \tfrac{r}{c}) - \delta(t'' - \tfrac{r}{c})\Big] \mathrm{d}t'' \right) \mathrm{d}t'.$$

Analogous to the zeroth-order case, a band limitation is applied by replacing the Dirac delta functions $\delta(t)$ with $h(t)$ (i.e. applying a low-pass filter),

$$h(t) * P_1(\tfrac{c}{r}t) = -H_0(t + \tfrac{r}{c}) - H_0(t - \tfrac{r}{c})$$
$$+ \tfrac{c}{r}\Big[H_1(t + \tfrac{r}{c}) - H_1(t - \tfrac{r}{c})\Big], \tag{29}$$

where the so-called band limited ramp function $H_1(t)$ corresponds to the second-order antiderivative of $h(t)$,

$$H_1(t) \coloneqq \int_{-\infty}^{t} \left(\int_{-\infty}^{t'} h(t'') \mathrm{d}t'' \right) \mathrm{d}t'. \tag{30}$$

This approach can be generalized to arbitrary orders n, where the radial function is represented as a superposition of higher-order discontinuities [21, Eq. (27)],

$$P_n(\tfrac{c}{r}t) = \sum_{k=0}^{n} \frac{b_n(k)}{k!} \left(\frac{c}{r}\right)^k \tag{31}$$
$$\times \Big[(-1)^{n-k}(t + \tfrac{r}{c})^k u(t + \tfrac{r}{c}) - (t - \tfrac{r}{c})^k u(t - \tfrac{r}{c})\Big],$$

where

$$b_n(k) = \frac{(n+k)!}{(n-k)!k!2^k}. \tag{32}$$

The kth-order discontinuities are described by $\frac{1}{k!}(t \pm \frac{r}{c})^k \cdot u(t \pm \frac{r}{c})$ which corresponds to the kth-order antiderivative of $\delta(t \pm \frac{r}{c})$. A band limitation is performed by replacing $\frac{1}{k!}(t \pm \frac{r}{c})^k \cdot u(t \pm \frac{r}{c})$ with the kth-order antiderivative of the prototype filter $h(t)$, which can be derived by successive integration,

$$H_k(t) = \int_{-\infty}^{t} H_{k-1}(t') \mathrm{d}t'. \tag{33}$$

The expression for the band-limited radial functions thus reads [21, Eq. (37)]

$$h(t) * P_n(\tfrac{c}{r}t) \tag{34}$$
$$= \sum_{k=0}^{n} b_n(k) (\tfrac{c}{r})^k \Big[(-1)^{n-k} H_k(t + \tfrac{r}{c}) - H_k(t - \tfrac{r}{c})\Big].$$

Note that this is a continuous-time representation which fully describes the time-domain behavior of the low-pass filtered radial functions. Due to its smoother transients, (34) can be sampled with reduced aliasing artifacts.

The spectral and temporal properties of the resulting radial filters highly depend on the prototype filter $h(t)$. Because of the uncertainty principle in signal processing, known as the Gabor principle [38], there is a trade-off between band limitation and temporal compactness. In general, longer impulse responses are likely to achieve stronger stop-band attenuation and thus less aliasing. The sinc kernel for instance constitutes an ideal low-pass filter which is achieved at the cost of infinite temporal extent (Fig. 4 center), and is therefore of limited practical interest. In this study, we attempt to reduce the aliasing artifacts as much as possible while keeping the radial filters to a reasonable length. As will be demonstrated in the following the compact temporal property of the radial filters can be maintained at the expense of moderate spectral deviations at high frequencies.

The authors have shown in [21, 37] that the prototype filters based on the Lagrange kernels meet the above criteria. Since the impulse response of a Lagrange kernel is described by polynomials, the antiderivatives $H_k(t)$ can be derived in closed form. In this study, we consider odd-order Lagrange polynomials which is known to be superior to even orders in terms of stop band attenuation [39, Sec. 5.3]. The polynomial order is denoted by $\mathcal{M}$. The Lagrange kernel is a continuous function defined within $\mathcal{M}+1$ intervals of equal lengths T_s. The intervals are defined by $\mathcal{M}+2$ nodal points which are equally distributed with respect to $t=0$,

$$\tfrac{t}{T_\mathrm{s}} = -\tfrac{\mathcal{M}+1}{2}, -\tfrac{\mathcal{M}-1}{2}, \ldots, \tfrac{\mathcal{M}+1}{2}. \tag{35}$$

For the μth interval ($\mu = 0, 1, \ldots, \mathcal{M}$),

$$\tfrac{t}{T_\mathrm{s}} \in [-\tfrac{\mathcal{M}+1}{2} + \mu,\ -\tfrac{\mathcal{M}+1}{2} + \mu + 1), \tag{36}$$

the impulse response is expressed as an $\mathcal{M}$-order polynomial [40],

$$h(t) = \frac{\prod_{\nu=0,\nu\neq\mathcal{M}-\mu}^{\mathcal{M}} (\frac{t}{T_\mathrm{s}} + \mathcal{M} - \mu - \nu)}{(\mathcal{M}-\mu)!\ \mu!\ (-1)^\mu}. \tag{37}$$

Outside these intervals ($|\frac{t}{T_\mathrm{s}}| > \frac{\mathcal{M}+1}{2}$), the impulse response is zero, thus constituting an (continuous-time) FIR filter. Figure 5 exemplarily depicts Lagrange kernels of different orders $\mathcal{M}$.

The antiderivatives $H_k(t)$ are derived by successively integrating $h(t)$ (cf. (24) and (33)). The integration constants have to be chosen in such a way that the resulting $H_k(t)$ is continuous at the nodes. The followings also have to be fulfilled beyond the outermost nodes,

$$H_k(t) = 0, \quad \frac{t}{T_\mathrm{s}} < -\frac{\mathcal{M}+1}{2} \tag{38}$$

$$H_k(t) = \frac{t^k}{k!}, \quad \frac{t}{T_\mathrm{s}} > \frac{\mathcal{M}+1}{2}. \tag{39}$$

As discussed in [21], these conditions can be satisfied only for $k \leq \mathcal{M}$. The maximum antiderivative order (denoted by $\mathcal{K}$) is thus limited by the polynomial order $\mathcal{K} \leq \mathcal{M}$. This implies that higher-order discontinuities have to be coped with Lagrange kernels of higher orders, which in turn increases the number of intervals and the length of the Lagrange kernel $(\mathcal{M}+1)\cdot T_\mathrm{s}$.

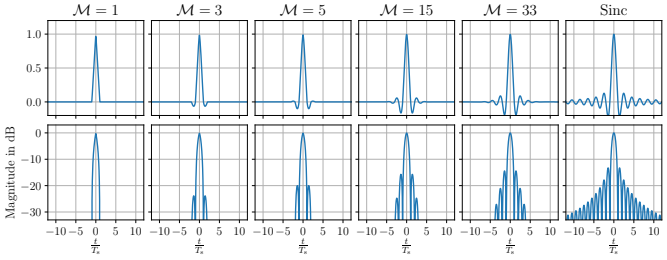

Fig. 5: Prototype filters $h(t)$ based on Lagrange kernels ($\mathcal{M} = 1, 3, 5, 15, 33$) and the sinc kernel (last column).

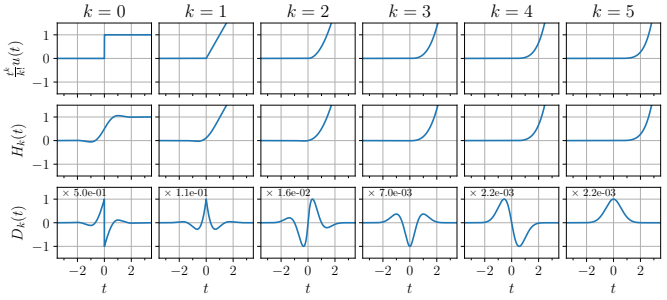

Fig. 6: Higher-order discontinuities $\frac{t^k}{k!}u(t)$, the band-limited functions $H_k(t)$ and the corresponding residual functions $D_k(t)$. The band limitation is performed based on the fifth-order Lagrange kernel. For a better visualization, the residual functions (bottom row) are depicted with differently scaled ordinates as indicated at the top left corners.

The higher-order antiderivatives $H_k(t)$ of the prototype filter are depicted in Fig. 6. The bottom row shows the difference between the fullband and band-limited discontinuities,

$$D_k(t) := H_k(t) - \frac{t^k}{k!}u(t), \tag{40}$$

which are referred to as the residual functions [32]. It is worth noting that the residual functions are also described by piecewise polynomials between the nodal points.

The following expression is useful for practical implementations,

$$h(t) * P_n(\tfrac{c}{r}t) = P_n(\tfrac{c}{r}t) + \sum_{k=0}^{n} \beta_n(k)(\tfrac{c}{r})^k \Big[(-1)^{n-k} D_k(t + \tfrac{r}{c}) - D_k(t - \tfrac{r}{c})\Big]. \tag{41}$$

This states that the band limitation can be carried out by superposing the scaled and delayed residuals $D_k(t)$ onto the original time-domain radial function $P_n(\frac{c}{r}t)$ around the discontinuities at $|t| = \frac{r}{c}$. It is worth noting that the superposition may be performed in the discrete-time domain where the samples in

the neighborhood of the discontinuities are updated according to the sampled residual functions. The zeroth-order spherical radial filter based on the Lagrange kernel is shown in Fig. 4 (right). Unlike the sinc kernel case, the radial filter has a finite length.

B. Cylindrical Radial Filter Design

The band limitation approach presented in the previous section (Sec. III-A) cannot be directly applied to cylindrical radial functions since the discontinuities at $|t| = \frac{r}{c}$ are of infinite magnitude. We employ the approximation (18) to circumvent this problem. A low-pass filtered cylindrical radial function is described by linearly combining the band-limited spherical radial functions (34),

$$\begin{aligned} h(t) * \frac{c}{\pi r} \frac{T_m(\frac{c}{r}t)}{\sqrt{1-(\frac{c}{r}t)^2}} \\ \approx \frac{c}{2r} \sum_{n=|m|}^{N} W_n \cdot (2n+1) K_n^m \\ \times \sum_{k=0}^{n} \beta_n(k) (\tfrac{c}{r}t)^k \Big[(-1)^{n-k} H_k(t+\tfrac{r}{c}) - H_k(t-\tfrac{r}{c}) \Big]. \end{aligned} \tag{42}$$

The FIR coefficients for the cylindrical radial filters are obtained by sampling the analytical time-domain expressions. The sampling frequency is set to $f_\mathrm{s} = 48\,\mathrm{kHz}$. The impulse responses of the proposed cylindrical radial filters are shown in Fig. 7. It can be seen that the components around $|t| = \frac{r}{c}$ are updated which corresponds to the residual functions $D_k(t \pm \frac{r}{c})$. The over-/undershoot is attributed to the transient properties of the Lagrange kernel.

The design accuracy of the cylindrical radial filters is evaluated in terms of spectral deviation defined as

$$\mathcal{E}_m(\omega) \coloneqq |\hat{\mathcal{H}}_m(\omega) - \mathcal{H}_m(\omega)| \tag{43}$$

where $\hat{\mathcal{H}}_m(\omega)$ denotes the spectrum of the cylindrical radial filter and $\mathcal{H}_m(\omega)$ the original cylindrical radial function $i^{-m} J_m(\frac{\omega}{c} r)$. Figure 8 depicts $\hat{\mathcal{H}}_m(\omega)$ in gray and $\mathcal{E}_m(\omega)$ in purple. Three different radial filter design methods are compared:

- Fig. 8(a) Sampling of the time-domain cylindrical radial functions (3). The FIR length is 139 samples. The aliasing artifacts dominate the high frequency spectrum. For even $m \geq 2$, the radial filter fails to model the mth-order zeros at $\omega = 0$, resulting in strong spectral deviation at low frequencies. Odd-order radial filters exhibit better accuracy at low frequencies benefiting from the odd symmetry (first-order zero at $\omega = 0$) of the FIR coefficients.
- Fig. 8(b) Sampling of the approximation (18). The FIR length is 139 samples. In comparison with Fig. 8(a), slight improvements are observed below $10\,\mathrm{kHz}$. The spectral deviation is however increased in the neighborhood of $\frac{f_\mathrm{s}}{2}$.
- Fig. 8(c) Sampling of the band-limited approximation (42). The band limitation is performed by using the fifth-order Lagrange kernel. This modifies six samples around each discontinuity (three on each side of the discontinuity). The FIR length is 145 samples. The spectral deviation is reduced in the entire frequency range. In particular, the improvements at low frequencies are considerable. The high-frequency spectrum of the cylindrical radial filter exhibits a roll-off which is attributed to the non-ideal low-pass filter characteristics of the Lagrange kernel.

The accuracy of the cylindrical radial filters is further examined in terms of normalized squared error (NSE),

$$\mathrm{NSE}_m \coloneqq 10 \log_{10} \left(\frac{\sum_l |\mathcal{E}_m(\omega_l)|^2}{\sum_l |\mathcal{H}_m(\omega_l)|^2} \right) \tag{44}$$

where ω_l are 2^{16} uniformly sampled frequencies within the Nyquist limit ($-\pi f_\mathrm{s} < \omega_l \leq \pi f_\mathrm{s}$). Figure 9 shows the NSE for varying approximation order N and radius r. The results for the sampled cylindrical radial functions are shown for comparison (indicated by black squares). As expected, the accuracy of the radial filter improves as the approximation order N increases. Including more spherical radial filters is more effective for higher m. For $r = 0.5\,\mathrm{m}$, doubling N from 15 to 30 reduces the NSE by $6.9\,\mathrm{dB}$ for $m = 0$ whereas by $11.2\,\mathrm{dB}$ for $m = 15$. The two subfigures demonstrate that the design accuracy largely depends on the radius r which determines the spectral components beyond the base band $|f| > \frac{f_\mathrm{s}}{2}$ and thus has a direct impact on the resulting aliasing artifacts. As r gets larger, higher N is required to achieve a comparable result. Note that if N is not sufficiently high, the proposed method might be inferior to the sampling of the cylindrical radial functions (e.g. choosing $N = 15$ for $r = 0.5\,\mathrm{m}$, $m = 13, 14, 15$).

IV. Local Wave Field Synthesis

The cylindrical radial filters designed in Sec. III can be used to model sound fields represented by cylindrical harmonic expansions. This not only includes configurations with cylindrical symmetries but also two-dimensional cases. In this section, the proposed cylindrical radial filters are employed for the implementation of WFS.

WFS is an analytical approach for spatial sound reproduction using loudspeaker arrays [41, 42]. The individual loudspeakers are driven in such a way that a desired sound field is physically reconstructed within an extended area. The theory of WFS bases on the high-frequency/far-field approximation of the Kirchhoff-Helmholtz integral equation [43]. The WFS driving function for the loudspeaker positioned at $\boldsymbol{x}_0 = (r_0 \cos\phi_0,\ r_0 \sin\phi_0,\ 0)^\mathrm{T}$ is given as the directional gradient of the desired sound field with respect to the unit vector $\boldsymbol{n}_0 = (\cos\phi_{\boldsymbol{n}_0}, \sin\phi_{\boldsymbol{n}_0}, 0)^\mathrm{T}$ which is normal to the array contour and points inward the listening area. Note that $\boldsymbol{x}_0$ and $\boldsymbol{n}_0$ are defined with different azimuth angles, ϕ_0 and $\phi_{\boldsymbol{n}_0}$ respectively. The driving function for a plane reads [44,

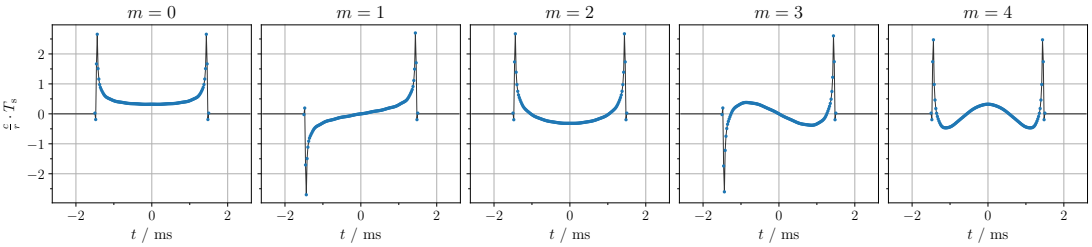

Fig. 7: The impulse responses of the proposed cylindrical radial filters (radius $r = 0.5\,\mathrm{m}$, sampling rate $f_\mathrm{s} = 48\,\mathrm{kHz}$, fifth-order Lagrange kernel). The filled circles indicate the FIR coefficients (145 samples).

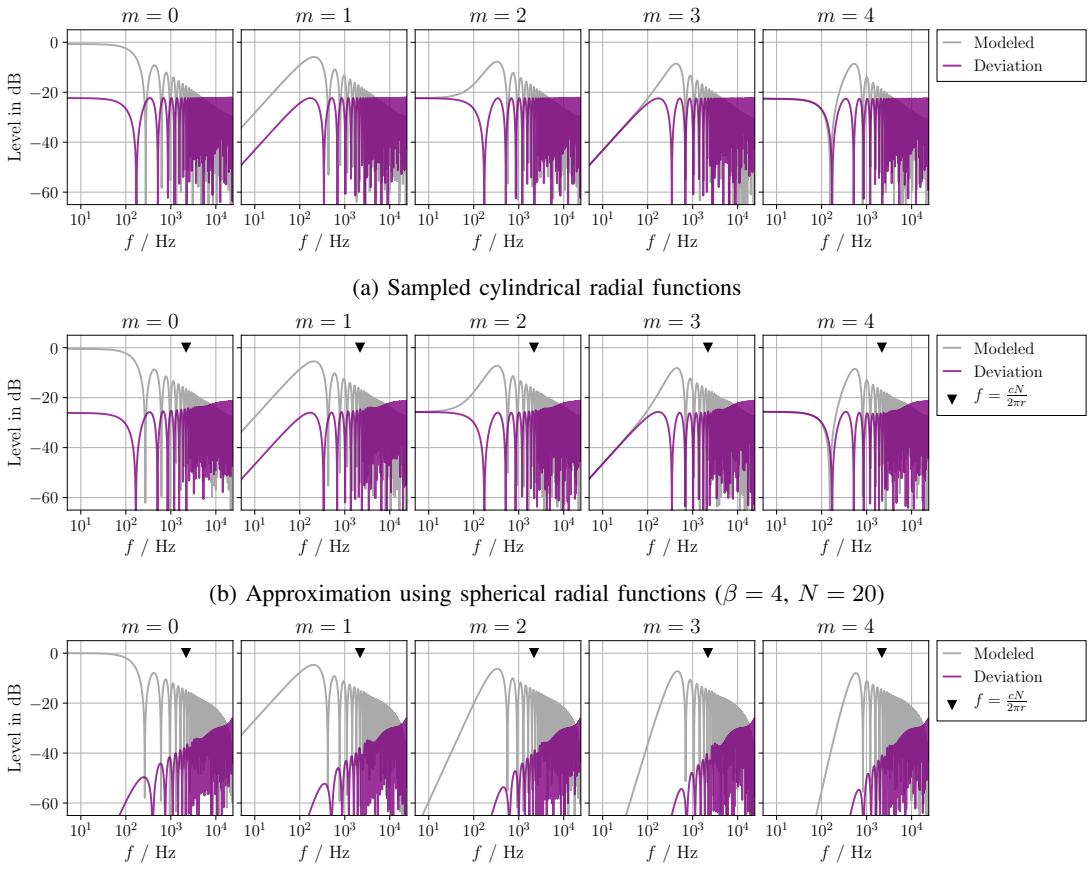

(a) Sampled cylindrical radial functions

(b) Approximation using spherical radial functions ($\beta = 4$, $N = 20$)

(c) Approximation using band limited spherical radial functions ($\beta = 4$, $N = 20$, fifth-order Lagrange kernel)

Fig. 8: Modal spectra of the cylindrical radial functions (radius $r = 0.5\,\mathrm{m}$, sampling rate $f_\mathrm{s} = 48\,\mathrm{kHz}$).

Sec. 2.4]

$$
\begin{aligned}
&d_{\mathrm{WFS}}(\boldsymbol{x}_0, t) \\
&= \Big[\sqrt{8\pi \|\boldsymbol{x}_0 - \boldsymbol{x}_{\mathrm{ref}}\|}\ \max\{\langle \boldsymbol{n}_0, \boldsymbol{n}_{\mathrm{pw}} \rangle, 0\} \\
&\quad \delta\left(t - \tfrac{r_0}{c} \cos(\phi_0 - \phi_{\mathrm{pw}})\right) \Big] * h_{\mathrm{pre}}(t), \qquad (45)
\end{aligned}
$$

where $h_{\mathrm{pre}}(t)$ denotes the so-called pre-equalization filter whose spectrum is $\sqrt{i\omega/c}$ ($+10\,\mathrm{dB/decade}$ and $+45°$ phase shift). The Dirac delta function $\delta\left(t - \frac{r_0}{c}\cos(\phi_0 - \phi_{\mathrm{pw}})\right)$ represents the sound field of the virtual plane wave evaluated at the loudspeaker position $\boldsymbol{x}_0$. Equation (45) constitutes a driving function for 2.5-dimensional WFS where a three-dimensional sound field is synthesized by a loudspeaker array distributed on a two-dimensional plane (e.g. circular and rectangular arrays). In such a 2.5-dimensional configuration, the desired sound field can be synthesized with a correct amplitude only on a predefined reference line. The term $\sqrt{\|\boldsymbol{x}_0 - \boldsymbol{x}_{\mathrm{ref}}\|}$ in (45) ensures that the synthesized sound field exhibits the correct amplitude at a fixed reference point $\boldsymbol{x}_{\mathrm{ref}}$. Here, we avoid to explicitly define the reference line $\boldsymbol{x}_{\mathrm{ref}}(\boldsymbol{x}_0)$ in order to keep the presented approach as straightforward as possible. The spatial window $\max\{\langle \boldsymbol{n}_0, \boldsymbol{n}_{\mathrm{pw}} \rangle, 0\} = \max\{\cos(\phi_{\boldsymbol{n}_0} - \phi_{\mathrm{pw}}), 0\}$ is a rectified cosine function whose maximum is unity at $\phi_{\boldsymbol{n}_0} = \phi_{\mathrm{pw}}$. The readers are referred to [45, 46] for a comprehensive treatment

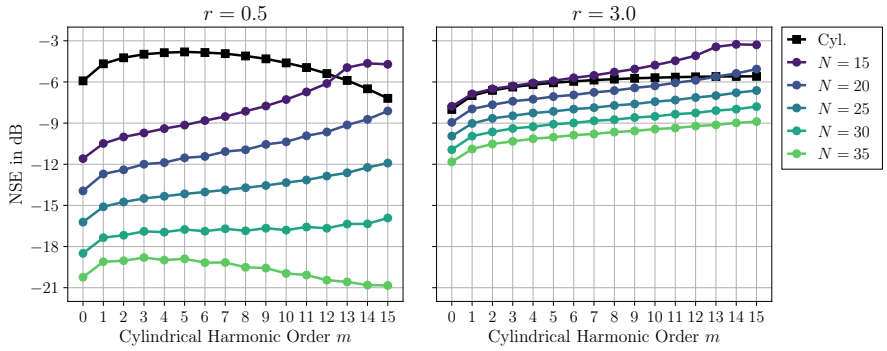

Fig. 9: Normalized squared error (44) of cylindrical radial filters. The filled circles indicate the results of the proposed method (15th-order Lagrange kernel) for varying design parameters (radius r, cylindrical harmonic order m, maximum spherical harmonic order N). The black squares (labeld 'Cyl.') show the results obtained by directly sampling the cylindrical radial functions without approximation and band-limitation (low-pass filtering).

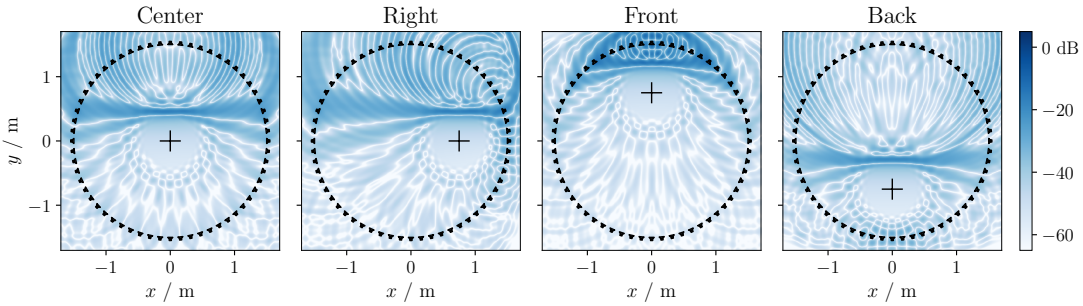

Fig. 10: LWFS of a plane wave impulse propagating in the direction $\boldsymbol{n}_{\text{pw}} = (0, -1, 0)^{\text{T}}$. Sixty monopole loudspeakers are placed on a circle with radius $r = 1.5\,\text{m}$. The snapshots are taken $1\,\text{ms}$ before the planar wavefront passes the reference point $\boldsymbol{x}_{\text{ref}}$ indicated by '+'. The logarithmic amplitude of the sound field is depicted according to the colormap shown on the right. The dynamic range of the displayed data is $70\,\text{dB}$, where the levels below $-65\,\text{dB}$ and above $+5\,\text{dB}$ are clipped.

of WFS.

In practical systems where real loudspeakers are placed with finite spacing, the synthesized sound field suffers from spatial aliasing artifacts which predominantly occur above the so-called spatial aliasing frequency. The spatial aliasing introduces spectral fluctuations at high frequencies with an approximate slope of $+10\,\text{dB/decade}$. The frequency response of the pre-equalization filter thus needs to be adjusted so that the slope of $+10\,\text{dB/decade}$ is flattened out above the spatial aliasing frequency [47, 48].

In local WFS (LWFS), the accuracy of the synthesized sound field is improved within a small pre-defined region which typically comes at the cost of stronger spatial aliasing artifacts elsewhere. A number of LWFS approaches have been proposed so far [49–51]. In this section, we consider the LWFS based on spatial band limitation [51], where the desired sound field is expanded with respect to a reference point in the spherical or cylindrical harmonic domain. The local accuracy of the synthesized sound field is improved by applying a modal band limitation. The size of the local sound field scales with the maximum harmonic order. This idea was first introduced for higher-order Ambisonics (HOA) [52], and later employed in WFS [51]. The LWFS driving functions were initially derived in the frequency domain [51]. Different versions of time-domain driving functions have been presented subsequently [22, 27, 53].

In order to derive the LWFS driving function for a virtual plane wave, we apply a spatial band limitation to the time-domain cylindrical harmonic expansion (2). The spatially band-limited plane wave is described by a truncated sum,

$$s_{M_s}(\boldsymbol{x}, t)$$

$$= \sum_{m=-M_s}^{M_s} \frac{c}{\pi r} \frac{T_m(\frac{c}{r}t)}{\sqrt{1-(\frac{c}{r}t)^2}} e^{im(\phi-\phi_{\text{pw}})} \tag{46}$$

$$= \int_0^{2\pi} \left[\sum_{m=-M_s}^{M_s} e^{im(\bar{\phi}-\phi_{\text{pw}})} \delta\left(t - \tfrac{r}{c}\cos(\phi-\bar{\phi})\right) \right] \mathrm{d}\bar{\phi}, \tag{47}$$

where M_s denotes the spatial bandwidth. The sound field on the horizontal plane ($\theta = \frac{\pi}{2}$) is considered. The second equality (47) converts the truncated cylindrical harmonic expansion to a plane wave expansion where the sound field is represented as a superposition of infinite number of plane waves $\delta\left(t - \frac{r}{c}\cos(\phi-\bar{\phi})\right)$ with $\bar{\phi} \in [0, 2\pi)$. The integration

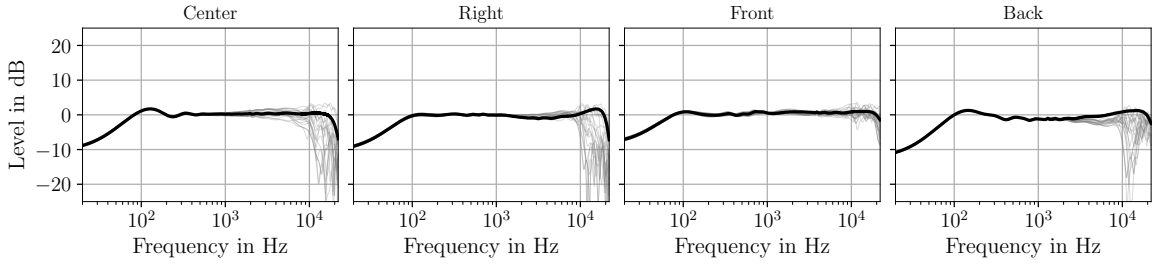

(a) With band limitation (proposed)

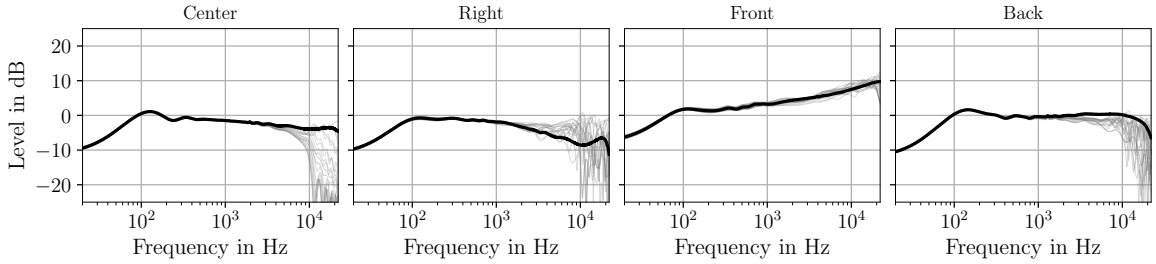

(b) Without band limitation (conventional)

Fig. 11: The frequency responses of the synthesized sound field on (thick) and off (thin) target positions. The cylindrical radial functions appearing in the LWFS driving functions (50) are realized by (a) the proposed band-limited design (based on 15th-order Lagrange kernel) and (b) the conventional design where the time-domain approximation (18) is sampled without band limitation. The off-target positions lie on a circle with radius $0.085\,\mathrm{m}$ centered at the respective reference point $\boldsymbol{x}_{\text{ref}}$. The frequency responses are evaluated for twenty equiangular positions.

variable $\bar{\phi}$ denotes the azimuth angle of each plane wave direction $\bar{\boldsymbol{n}} = (\cos\bar{\phi}, \sin\bar{\phi}, 0)^{\mathrm{T}}$. The truncated Fourier series $\sum_{m=-M_s}^{M_s} e^{im(\bar{\phi}-\phi_{\text{pw}})}$ represents the corresponding amplitude.

The time-domain LWFS driving function is derived by applying the conventional driving function (45) to the individual plane waves (azimuth $\bar{\phi}$) composing the spatially band-limited version of the original plane wave (azimuth ϕ_{pw}) (47), yielding

$$\begin{aligned} & d_{\text{LWFS}}(\boldsymbol{x}_0, t) \\ &= \sqrt{8\pi r_0} \cdot h_{\text{pre}}(t) \\ &\quad * \int_0^{2\pi} \Bigg[\Bigg(\sum_{m=-M_s}^{M_s} e^{im(\bar{\phi}-\phi_{\text{pw}})} \Bigg) \Bigg(\sum_{m=-M_a}^{M_a} \mathring{a}_m(\phi_{\boldsymbol{n}_0}) e^{im\bar{\phi}} \Bigg) \\ &\qquad \delta\left(t - \tfrac{r_0}{c}\cos(\phi_0 - \bar{\phi})\right) \Bigg] \mathrm{d}\bar{\phi} \qquad (48) \\ &= \sqrt{8\pi r_0} \cdot h_{\text{pre}}(t) \\ &\quad * \int_0^{2\pi} \Bigg[\sum_{m=M}^{M} \mathring{d}_m(\phi_{\text{pw}}, \phi_{\boldsymbol{n}_0}) e^{im\bar{\phi}} \delta\left(t - \tfrac{r_0}{c}\cos(\phi_0 - \bar{\phi})\right) \Bigg] \mathrm{d}\bar{\phi} \qquad (49) \\ &= \sqrt{8\pi r_0} \cdot h_{\text{pre}}(t) \\ &\quad * \Bigg[\sum_{m=-M}^{M} \mathring{d}_m(\phi_{\text{pw}}, \phi_{\boldsymbol{n}_0}) \frac{c}{\pi r_0} \frac{T_m(\frac{c}{r_0}t)}{\sqrt{1-(\frac{c}{r_0}t)^2}} e^{im\phi_0} \Bigg]. \qquad (50) \end{aligned}$$

The second sum in (48) represents the spatial window approximated by a truncated Fourier series with respect to $\bar{\phi}$ [27, Eq. (9) and (10)],

$$\max\{\langle \boldsymbol{n}_0, \bar{\boldsymbol{n}}\rangle, 0\} \approx \sum_{m=-M_a}^{M_a} \mathring{a}_m(\phi_{\boldsymbol{n}_0}) e^{im\bar{\phi}}, \qquad (51)$$

where the coefficient are given as

$$\mathring{a}_m(\phi_{\boldsymbol{n}_0}) = \begin{cases} \frac{(-1)^{m/2}}{\pi(1-m^2)} e^{-im\phi_{\boldsymbol{n}_0}}, & m \text{ even} \\ \frac{1}{4} e^{-im\phi_{\boldsymbol{n}_0}}, & m \pm 1 \\ 0, & \text{otherwise.} \end{cases} \qquad (52)$$

In the LWFS driving function (48), the spatial window is applied to each plane wave. This is carried in the angular domain by multiplying the truncated expansions of the spatial window (51) and the plane wave amplitude represented by the plane wave expansion (47). This results in a single sum in the second equality (49) where $\mathring{d}_m(\phi_{\text{pw}}, \phi_{\boldsymbol{n}_0})$ is the convolution (denoted by $*_m$) of the respective coefficients in the Fourier-series domain,

$$\mathring{d}_m(\phi_{\text{pw}}, \phi_{\boldsymbol{n}_0}) = e^{-im\phi_{\text{pw}}} *_m \mathring{a}_m(\phi_{\boldsymbol{n}_0}). \qquad (53)$$

The maximum order of the driving function $\mathring{d}_m(\phi_{\text{pw}}, \phi_{\boldsymbol{n}_0})$ is therefore the sum of the modal bandwidth describing the sound field (47) and the truncation order of the spatial window (51), i.e. $M = M_s + M_a$. The third equality (50) converts the plane wave expansion back into a cylindrical harmonic expansion. Since the reference point is always the expansion center $\boldsymbol{x}_{\text{ref}} = \boldsymbol{0}$, the amplitude correction term reads $\sqrt{8\pi\|\boldsymbol{x}_0 - \boldsymbol{x}_{\text{ref}}\|} = \sqrt{8\pi r_0}$. The pre-equalization filter $h_{\text{pre}}(t)$ is unchanged.

In order to demonstrate the benefit of using the radial filter design presented in Sec. III, we implement the LWFS driving functions (50) and investigate the synthesized sound fields by means of numerical simulation. The sound field of a virtual plane wave is considered which propagates in the $-y$ direction (i.e. $\boldsymbol{n}_{\mathrm{pw}} = (0, -1, 0)^{\mathrm{T}}$). A circular loudspeaker array is considered which has the radius of $1.5\,\mathrm{m}$ and consists of 60 ideal monopole sources. An ideal free-field condition is assumed. The cylindrical radial filters in (50) are realized according to the approach presented in Sec. III-B. The sampling frequency is set to $f_{\mathrm{s}} = 48\,\mathrm{kHz}$. The 15th-order Lagrange kernel is used for the temporal bandwidth limitation (i.e. anti-alias filtering). The Kaiser-Bessel window ($\beta = 4$) was used for the approximation (42). Four different reference points are chosen:

- Center: $(0,\ 0,\ 0)^{\mathrm{T}}$
- Right: $(0.75,\ 0,\ 0)^{\mathrm{T}}$
- Front: $(0,\ 0.75,\ 0)^{\mathrm{T}}$
- Back: $(0, -0.75,\ 0)^{\mathrm{T}}$

The driving function (50) is computed for translated coordinate systems where the reference points coincide with the origin. The cylindrical harmonic expansion of the sound field is limited to $M_s = 15$ and the spatial window (51) is expanded by the Fourier series (51) up to $M_a = 20$. The modal bandwidth of the driving function is thus $M = M_s + M_a = 35$. The maximum spherical harmonic order N for the approximation (18) is set to $N = 30$. The pre-equalization filter $h_{\mathrm{pre}}(t)$ is realized as a linear phase FIR filter (257 taps), omitting the phase response ($+45°$) of the ideal pre-equalization filter ($\sqrt{i\omega/c}$).

The synthesized sound fields are shown in Fig. 10. Those are the snapshots $1\,\mathrm{ms}$ before the arrival of the plane wave at the reference point (corresponding to a propagation distance of $0.343\,\mathrm{m}$). For a better visualization of the spatial structure, the driving functions are driven with a low pass filtered impulse (sixth-order Butterworth filter with cut-off frequency at $5\,\mathrm{kHz}$). It can be seen that, in addition to the original plane wave, small spatio-temporal components arrive from different azimuth angles which is attributed to the spatial band limitation. Irrespective of the reference point, the spatial structure of the synthesized sound field is very similar.

The frequency responses of the synthesized sound fields are depicted in Fig. 11. The cylindrical radial filters are implemented based on the approximation (18) where the Kaiser-Bessel window ($\beta = 4$) is used for modal smoothing. The results with and without band-limitation (anti-aliasing) are shown in Fig. 11(a) and Fig. 11(b), respectively. The proposed method achieves a flat frequency response from $100\,\mathrm{Hz}$ to $1\,\mathrm{kHz}$, whereas the conventional method (without band limitation) results in a spectral slope that varies with the reference point. Low frequency roll-offs are observed in all cases which is due to the finite spatial extent of the loudspeaker array. Since WFS is based on the high-frequency approximation of the Kirchhoff-Helmholtz integral equation, the synthesized sound fields commonly exhibit spectral deviations in low frequencies where the wavelength is larger than the overall size of the array [48]. The thin gray lines show the frequency responses evaluated on a circle (radius $85\,\mathrm{mm}$) centered at each $\boldsymbol{x}_{\mathrm{ref}}$. These show the spectral variability of the sound field at off-target positions which is influenced by the spatial band limitation as well as the spatial aliasing artifacts.

V. CONCLUSION

In this paper, we presented a time-domain design of the cylindrical radial filters where the radial and frequency dependencies of cylindrical harmonic expansions are modeled by FIR filters. It was shown that a straightforward time-domain sampling of the cylindrical radial functions inevitably causes severe aliasing artifacts in the frequency domain. This is attributed to the discontinuities of the time-domain cylindrical radial functions which exhibit an infinite bandwidth. Since the discontinuities are unbounded, it is not trivial to apply a band limitation. In order to circumvent this problem, we exploited an approximation of the cylindrical radial functions which is expressed as a linear combination of the spherical radial functions. Since a band-limited design is known for the spherical radial filters, the cylindrical radial filters are constructed by combining the spherical radial filters with reduced aliasing artifacts. The improved accuracy of the proposed cylindrical radial filters was demonstrated by examining the spectral deviations and the normalized squared errors. The cylindrical radial filters were used to implement the local wave field synthesis based on spatial band limitation. The synthesized sound fields were shown to benefit from the improved radial filter design. The presented approach is expected to be used in other spatial signal processing tasks where cylindrical configurations are under consideration or a two-dimensional model (e.g. height invariance) of the sound field appears appropriate. This includes not only the numerical simulation of acoustic fields but also applications such as sound field analysis, sound field control, and active noise cancellation where a discrete-time model of the sound field has to be plugged in to the respective algorithm.

REFERENCES

[1] E. Williams, *Fourier Acoustics: Sound Radiation and Nearfield Acoustical Holography*. London, UK: Academic Press, 1999.

[2] N. A. Gumerov and R. Duraiswami, *Fast Multipole Methods for the Helmholtz Equation in Three Dimensions*. Oxford, UK: Elsevier, 2005.

[3] H. Teutsch, *Modal Array Signal Processing: Principles and Applications of Acoustic Wavefield Decomposition*. Berlin, Germany: Springer, 2007.

[4] A. Kuntz, *Wave Field Analysis Using Virtual Circular Microphone Arrays*. Munich, Germany: Verlag Dr. Hut, 2009.

[5] J. Ahrens, *Analytic Methods of Sound Field Synthesis*. Berlin, Germany: Springer, 2012.

[6] B. Rafaely, *Fundamentals of Spherical Array Processing*. Berlin, Germany: Springer, 2015.

[7] H. Pomberger, "Angular and radial directivity control for spherical loudspeaker arrays," Master's thesis, University of Music and Dramatic Arts, Graz, Austria, 2008.

[8] F. Zotter, "Analysis and synthesis of sound-radiation with spherical arrays," Ph.D. dissertation, University of Music and Performing Arts, Graz, Austria, 2009.

[9] S. Lösler and F. Zotter, "Comprehensive radial filter design for practical higher-order Ambisonic recording," in *Proc. 41st German Annu. Conf. Acoust. (DAGA)*, Nuremberg, Germany, Mar. 2015, pp. 452–455.

[10] S. Spors, V. Kuscher, and J. Ahrens, "Efficient realization of model-based rendering for 2.5-dimensional near-field compensated higher order Ambisonics," in *Proc. IEEE Workshop Appl. Signal Process. Audio Acoust. (WASPAA)*, New Paltz, USA, Oct. 2011, pp. 61–64.

[11] N. Hahn, F. Schultz, and S. Spors, "Spatio-temporal properties of simulated impulse responses on a rigid sphere," in *Proc. 47th German Annu. Conf. Acoust. (DAGA)*, Wien, Austria, Aug. 2021.

[12] O. M. Buyukdura and S. S. Koc, "Two alternative expressions for the spherical wave expansion of the time domain scalar free-space Green's function and an application: Scattering by a soft sphere," *J. Acoust. Soc. Am. (JASA)*, vol. 101, no. 1, pp. 87–91, Jan. 1997.

[13] R. Baumgartner, "Time domain fast-multipole translation for ambisonics," Master's thesis, University of Music and Dramatic Arts, Graz, Austria, 2011.

[14] J. Li and B. Shanker, "Time-dependent Debye-Mie series solutions for electromagnetic scattering," *IEEE Trans. Antennas Propag.*, vol. 63, no. 8, pp. 3644–3653, Aug. 2015.

[15] N. Hahn and S. Spors, "Physical properties of modal beamforming in the context of data-based sound reproduction," in *Proc. 139th Audio Eng. Soc. (AES) Conv.*, New York, NY, USA, Oct. 2015, paper 9468.

[16] M. Poletti, T. D. Abhayapala, and P. D. Teal, "Time domain description of spatial modes of 2D and 3D free-space Greens functions," in *Proc. Audio Eng. Soc. (AES) Conf.*, Guildford, UK, Jul. 2016.

[17] F. Ma, W. Zhang, and T. D. Abhayapala, "Reference signal generation for broadband ANC systems in reverberant rooms," in *IEEE Int. Conf. Acoust. Speech Signal Process. (ICASSP)*, Calgary, Canada, Apr. 2018, pp. 216–220.

[18] N. Hahn and S. Spors, "Time-domain representations of a plane wave with spatial band-limitation in the spherical harmonics domain," in *Proc. 45th German Annu. Conf. Acoust. (DAGA)*, Rostock, Germany, Mar. 2019, pp. 1434–1439.

[19] N. Hahn, F. Schultz, and S. Spors, "Time domain sampling of the radial functions in spherical harmonics expansions," *IEEE Trans. Signal Process.*, vol. 69, pp. 4502–4512, Jun. 2021.

[20] N. Hahn and S. Spors, "Discrete time modeling of spherical harmonics expansion by using band-limited step functions," in *Proc. 46th German Annu. Conf. Acoust. (DAGA)*, Hannover, Germany, Mar. 2020.

[21] N. Hahn, F. Schultz, and S. Spors, "Higher-order anti-derivatives of band-limited step functions for the design of radial filters in spherical harmonics expansions," in *Proc. 23rd Int. Conf. Digital Audio Effects (DAFx)*, Vienna, Austria, Sep. 2021.

[22] N. Hahn, F. Winter, and S. Spors, "Synthesis of a spatially band-limited plane wave in the time-domain using wave field synthesis," in *Proc. Eur. Signal Process. Conf. (EUSIPCO)*, Kos Island, Greece, Aug. 2017, pp. 673–677.

[23] G. B. Arfken and H. J. Weber, *Mathematical Methods for Physicists*. Burlington, MA, USA: Academic Press, 2005.

[24] M. Abramowitz and I. A. Stegun, *Handbook of Mathematical Functions: with Formulas, Graphs, and Mathematical Tables*. New York, NY, USA: Dover, 1964.

[25] F. W. J. Olver, D. W. Lozier, R. F. Boisvert, and C. W. Clark, *NIST Handbook of Mathematical Functions*. New York, NY, USA: Cambridge Univ. Press, 2010.

[26] B. Girod, R. Rabenstein, and A. Stenger, *Signals and Systems*. New York, NY, USA: Wiley, 2001.

[27] N. Hahn, F. Winter, and S. Spors, "2.5D local wave field synthesis of a virtual plane wave using a time domain representation of spherical harmonics expansion," in *Proc. 23rd Int. Cong. Acoust. (ICA)*, Aachen, Germany, Sep. 2019, pp. 1132–1139.

[28] D. B. Ward and T. D. Abhayapala, "Reproduction of a plane-wave sound field using an array of loudspeakers," *IEEE Trans. Speech Audio Process.*, vol. 9, no. 6, pp. 697–707, Sep. 2001.

[29] J. Kaiser and R. Schafer, "On the use of the $I_0 - \sinh$ window for spectrum analysis," *IEEE Trans. Acoust. Speech Sig. Process.*, vol. 28, no. 1, pp. 105–107, Feb. 1980.

[30] T. Stilson and J. O. Smith, "Alias-free digital synthesis of classic analog waveforms." in *Proc. Int. Comput. Music Conf.*, Hong Kong, Aug. 1996.

[31] E. Brandt, "Hard sync without aliasing," in *Proc. Int. Computer Music Conf.*, Havana, Cuba, Sep. 2001, pp. 365–368.

[32] V. Välimäki and A. Huovilainen, "Antialiasing oscillators in subtractive synthesis," *IEEE Signal Process. Mag.*, vol. 24, no. 2, pp. 116–125, Mar. 2007.

[33] V. Välimäki, J. Pekonen, and J. Nam, "Perceptually informed synthesis of bandlimited classical waveforms using integrated polynomial interpolation," *J. Acoust. Soc. Am.*, vol. 131, no. 1, pp. 974–986, Jan. 2012.

[34] F. Esqueda, V. Välimäki, and S. Bilbao, "Rounding corners with BLAMP," in *Proc. Int. Conf. Digit. Audio Effects (DAFx)*, Brno, Czech Republic, Sep. 2016, pp. 121–128.

[35] ——, "Antialiased soft clipping using an integrated bandlimited ramp," in *Proc. 24th Eur. Signal Process. Conf. (EUSIPCO)*, Budapest, Hungary, Aug. 2016, pp. 1043–1047.

[36] F. Esqueda, S. Bilbao, and V. Välimäki, "Aliasing reduction in clipped signals," *IEEE Trans. Signal Process.*, vol. 64, no. 20, pp. 5255–5267, Jun. 2016.

[37] N. Hahn, F. Schultz, and S. Spors, "Time domain radial filter design for spherical waves," Manuscript submitted for publication.

[38] D. Gabor, "Theory of communication. part 1: The analysis of information," *J. Inst. Elect. Eng. – Part III: Radio & Commun. Eng.*, vol. 93, no. 26, pp. 429–441, 1946.

[39] A. Franck, "Efficient algorithms for arbitrary sample rate conversion with application to wave field synthesis," Ph.D. dissertation, Ilmenau University of Technology, Ilmenau, Germany, Nov. 2012.

[40] A. Franck and K. Brandenburg, "A closed-form description for the continuous frequency response of lagrange interpolators," *IEEE Sig. Process. Lett.*, vol. 16, no. 7, pp. 612–615, Apr. 2009.

[41] A. J. Berkhout, D. de Vries, and P. Vogel, "Acoustic control by wave field synthesis," *J. Acoust. Soc. Am. (JASA)*, vol. 93, no. 5, pp. 2764–2778, May 1993.

[42] S. Spors, R. Rabenstein, and J. Ahrens, "The theory of wave field synthesis revisited," in *Proc. 124th Audio Eng. Soc. (AES) Conv.*, Amsterdam, The Netherlands, May 2008, paper 7358.

[43] F. Zotter and S. Spors, "Is sound field control determined at all frequencies? how is it related to numerical acoustics?" in *Proc. 52nd Int. Audio Eng. Soc. (AES) Conf. Sound Field Control*, Guildford, UK, Sep. 2013.

[44] F. Schultz, "Sound Field Synthesis for Line Source Array Applications in Large-Scale Sound Reinforcement," Ph.D. dissertation, Rostock, Germany, Jun. 2016.

[45] E. W. Start, "Direct sound enhancement by wave field synthesis," Ph.D. dissertation, Delft University of Technology, Delft, The Netherlands, Jun. 1997.

[46] G. Firtha, "A generalized wave field synthesis framework with application for moving virtual sources," Ph.D. dissertation, Budapest University of Technology and Economics, Budapest, Hungary, Apr. 2019.

[47] E. N. G. Verheijen, "Sound reproduction by wave field synthesis," Ph.D. dissertation, Delft University of Technology, Delft, The Netherlands, Jan. 1998.

[48] S. Spors and J. Ahrens, "Analysis and improvement of pre-equalization in 2.5-dimensional wave field synthesis," in *Proc. 128th Audio Eng. Soc. (AES) Conv.*, London, UK, May 2010, paper 8121.

[49] ——, "Local sound field synthesis by virtual secondary sources," in *Proc. 40th Int. Audio Eng. Soc. (AES) Conf. Spatial Audio*, Tokyo, Japan, Oct. 2010.

[50] S. Spors, K. Helwani, and J. Ahrens, "Local sound field synthesis by virtual acoustic scattering and time-reversal," in *Proc. 131th Audio Eng. Soc. (AES) Conv.*, New York, USA, Oct. 2011, paper 8529.

[51] N. Hahn, F. Winter, and S. Spors, "Local wave field synthesis by spatial band-limitation in the circular/spherical harmonics domain," in *Proc. 140th Audio Eng. Soc. (AES) Conv.* Audio Engineering Society, May 2016, paper 9596.

[52] J. Ahrens and S. Spors, "An analytical approach to sound field reproduction with a movable sweet spot using circular distributions of loudspeakers," in *Proc. Int. Conf. Acoust. Speech Signal Process. (ICASSP)*, Taipei, Taiwan, Apr. 2009.

[53] F. Winter, N. Hahn, and S. Spors, "Time-domain realisation of model-based rendering for 2.5D local wave field synthesis using spatial bandwidth-limitation," in *Proc. Eur. Signal Process. Conf. (EUSIPCO)*, Kos Island, Greece, Aug. 2017, pp. 688–692.